

Landslide investigations in the northwest section of the lesser Khingan range in China using combined HDR and GPR methods

Zhaoguang Hu¹ · Wei Shan¹

Received: 4 January 2015 / Accepted: 22 September 2015 / Published online: 3 October 2015
© The Author(s) 2015. This article is published with open access at Springerlink.com

Abstract In the northwest section of the lesser Khingan range, located in the high-latitude permafrost region of northeast China, landslides are a frequent occurrence, due to permafrost melting and atmospheric precipitation. High-density resistivity (HDR) and ground-penetrating radar (GPR) methods are based on soil resistivity values and characteristics of radar wave reflection, respectively. The combination of these methods, together with geological drilling, can be used to determine the stratigraphic distribution of this region, which will allow precise determination of the exact location of the sliding surface of the landslide. Field test results show that the resistivity values and radar reflectivity characteristics of the soil in the landslide mass largely differ from those of the soil outside the mass. The apparent resistivity values exhibit abrupt layering at the position of the sliding surface, with a sudden decrease in apparent resistivity. In addition, the radar wave shows strong reflection at the position of the sliding surface, where the amplitude of the radar wave exhibits a sudden increase. Drilling results indicate that the soil has high water content at the location of the sliding surface of the landslide mass in the study area, which is entirely consistent with the GPR and HDR results. Thus, in practice, sudden changes in apparent resistivity values and abnormal radar wave reflection can be used as a basis for determining the location of sliding surfaces of landslide masses in this region.

Keywords Landslide · Drilling · High-density resistivity (HDR) · Ground-penetrating radar (GPR) · Sliding surface

Introduction

In recent decades, geophysical investigations for assessing stratigraphic distribution have become a common tool in geological research. In situ geophysical techniques are able to measure physical parameters directly or indirectly linked with the lithological, hydrological and geotechnical characteristics of the terrains related to the movement (McCann and Forster 1990; Hack 2000; Benedetto et al. 2013). These techniques, less invasive than direct ground-based techniques (i.e., drilling, inclinometer, laboratory tests), provide information integrated on a greater volume of the soil, thus overcoming the point-scale feature of classical geotechnical measurements. Among the in situ geophysical techniques, the high-density resistivity (HDR) and ground-penetrating radar (GPR) methods have been increasingly applied for landslide investigation (McCann and Forster 1990; Malehmir et al. 2013; Timothy et al. 2014).

HDR is based on the measure of electrical resistivity and can provide 2D and 3D images of its distribution in the subsoil. It is one of the standard methods of geophysical prospecting for investigating shallow geological problems (Cardarelli et al. 2003; Yamakawa et al. 2010; Donohue et al. 2011; Sauvin et al. 2014). Current applications of HDR focus on landslide recognition and permafrost detection, while investigations on debris thickness in arctic and alpine environments are comparatively sparse (Carpentier et al. 2012; Donohue et al. 2011; Perrone et al. 2014). GPR is based on the measure of reflection of radar waves in the subsoil, and is largely focused on the fields of natural resource exploration, hydrogeology, engineering

✉ Wei Shan
shanwei456@163.com

¹ Institute of Cold Regions Science and Engineering, Northeast Forestry University, Harbin 150040, Heilongjiang, China

and archaeological investigation (Sass 2007; Sass et al. 2008; Schrott and Sass 2008; Zajc et al. 2014).

HDR and GPR are useful for determining characteristics such as the landslide main body, geometry, and surface of rupture, and have been used in landslide investigations since the late 1970s (Hack 2000; Havenith et al. 2000; Bichler et al. 2004; Drahor et al. 2006; Rhim and Chul 2011). However, the applicability of the various geophysical methods, including regional limitations and reliability, in estimating stratum thickness and sliding surface location of landslides in high-latitude permafrost regions in northeast China has not been addressed in detail. Applications of geophysical prospecting on landslides in cold regions of the lesser Khingan range of China have been rare.

Using landslide K178 + 530 as an example, in this paper we present a combination of traditional methods (drilling and mapping) and geophysical techniques (HDR and GPR) applied to the landslide in the lesser Khingan range of northeast China in order to investigate the thickness and internal structure of the landslides that occur frequently as a result of melting permafrost and atmospheric precipitation, in an effort to ascertain the applicability of HDR and GPR on this regional type of landslide.

Study area

The Bei'an-Heihe Highway is located in the northwest section of the lesser Khingan range of northeast China, between east longitude 127°17'31"–127°21'24" and north latitude 49°30'57"–49°41'50" (Fig. 1). This area is situated on the southern fringe of China's high-latitude permafrost region and has typical periglacial landforms. The discontinuous permafrost in this region belongs to residual paleoglacial deposition and is currently in degradation. Hence, the geological conditions are extremely unstable (Shan et al. 2015). A 2010 survey conducted in conjunction with a project for widening the Bei'an-Heihe road and construction of the Bei'an-Heihe Highway showed that four landslides occurred in the K177 + 400–K179 + 200 section within 10 m of the left of the roadbed, with a combined surface area of over 2000 m², as illustrated in Fig. 1 (the four landslides are located in the A, B, C and D positions, respectively, with C indicating landslide K178 + 530). Figure 1 shows the geologic and geomorphic map of the landside road section of the study area plotted from a field survey conducted in June 2010.

The geological structure of the study area belongs to the Khingan–Haixi fold belt. From the bottom up, the stratigraphy comprises Cretaceous mudstone, Tertiary pebbly sandstone, silty mudstone and powdery sandstone. From the late Tertiary to the early Quaternary, the lesser Khingan range experienced block uplift. Due to long-term erosion

and leveling, loose sediments on the summit and slope of the hills have gradually thinned, and the current residual layer is generally only 1–2 m thick. The loose deposits accumulate mainly in the basin and valley areas between mountains, with a thickness of about 10 m. The soil is mainly composed of clayey silt, mild clay and gravelly sand, and the surface is covered with a relatively thick layer of grass peat and turf. The surface vegetation is grassland and woodland, and there are inverted trees in the woodlands.

Landslide K178 + 530 on the Bei'an-Heihe Highway is located at the widened embankment on the left side of the road, as shown in Fig. 2. The roadbed and surface soil slide together along the valley, with the farthest slip 200 m from the road. The landslide mass has a flat tongue shape, is 20–30 m wide, and covers an area of approximately 6000 m². The distance between the leading and trailing edges is 200 m. The height of the leading edge is 254 m, and that of the trailing edge is 285 m. The leading edge of the landslide pushes the soil on the original ground surface and slides forward together with it. The trailing edge of the landslide has an arc-shaped dislocation, which is located inside the range of the widened embankment.

Four engineering geological boreholes were drilled into the K178 + 530 section for prospecting purposes. The depths of the boreholes ranged from 14 to 26 m, and the borehole distribution is shown in Fig. 3. The drilling revealed soil distribution along the profile, from top to bottom, of Quaternary loose soils, Tertiary pebbly sandstones, siltstones and Cretaceous mudstones. The geological profile is illustrated in Fig. 5.

Embankment: yellow, mainly composed of loosely mixed Tertiary pebbly sandstones, Cretaceous mudstones and sandy mudstones; soil is loose when dry, plastic when saturated with water. Clay: yellow, soft and plastic, of high strength and toughness when dry. The upstream region of the landslide mass has a depth distribution of 1.5–3.8 m. The downstream region has depth distribution of 0–6.7 m, and there is more than one sandwiched grit layer; the thickness of a single layer is approximately 1–10 cm, which greatly enhances the water seepage capacity of the soil.

Tertiary pebbly sandstones: distributed in the embankment at a depth of 2.0–3.4 m and in the upstream region of the landslide mass at a depth of 3.8–4.5 m, all weathered, composed mainly of feldspar stone and mineral sands, well-graded, highly permeable. Fully weathered siltstones: yellow, distributed in the upstream region of the landslide mass at a depth of 4.5–9.7 m, sandy, of bedding structure and poor water seepage capacity.

Fully weathered mudstone: yellow or gray-green, pelite, of layered structure, easy to soften with water, with poor water seepage capacity. Strongly weathered mudstones:

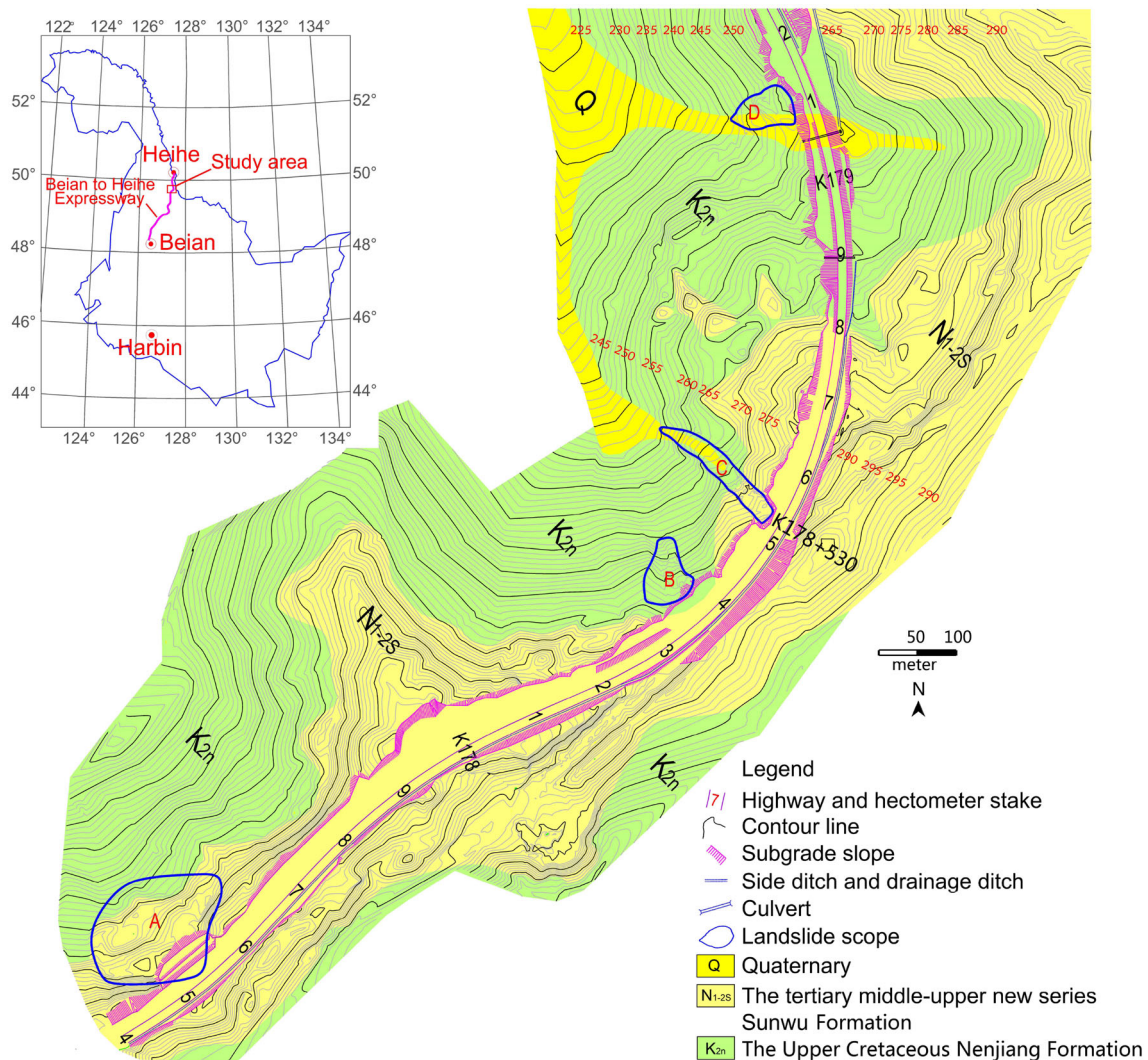


Fig. 1 Geologic and geomorphic map of the field area (June 2010)

dark gray, pelite, of layered structure, weakly cemented rock. Moderately weathered mudstones: brown, black and gray, pelite, layered structure.

Methods

In this paper, we present combination HDR and GPR geophysical techniques applied to landslide K178 + 530 on the Bei'an-Heihe Highway in the lesser Khingan range of northeast China. Survey lines were established as shown in Fig. 4.

HDR method

The instrument used in this study was the WGMD-9 Super HDR system (Chongqing Benteng Digital Control

Technical Institute, Chongqing, China). With this system, the WDA-1 super digital direct current electric device is used as measurement and control host, and with the optional WDZJ-4 multi-channel electrode converter, centralized high-density cables and electrodes, centralized two-dimensional HDR measurement can be achieved. The inversion of the apparent resistivity data sets that were obtained was performed using the RES2DINV software package, which produces a two-dimensional subsurface model from the apparent resistivity pseudo-section (Loke and Barker 1996). Data were acquired using a Wenner configuration. The method is based on the smoothness-constrained least-squares inversion of pseudo-section data (Tripp et al. 1984; Sasaki 1992; Loke and Barker 1996). In this algorithm, the subsurface is divided into rectangular blocks of constant resistivity. The resistivity of each block is then evaluated by minimizing the difference between

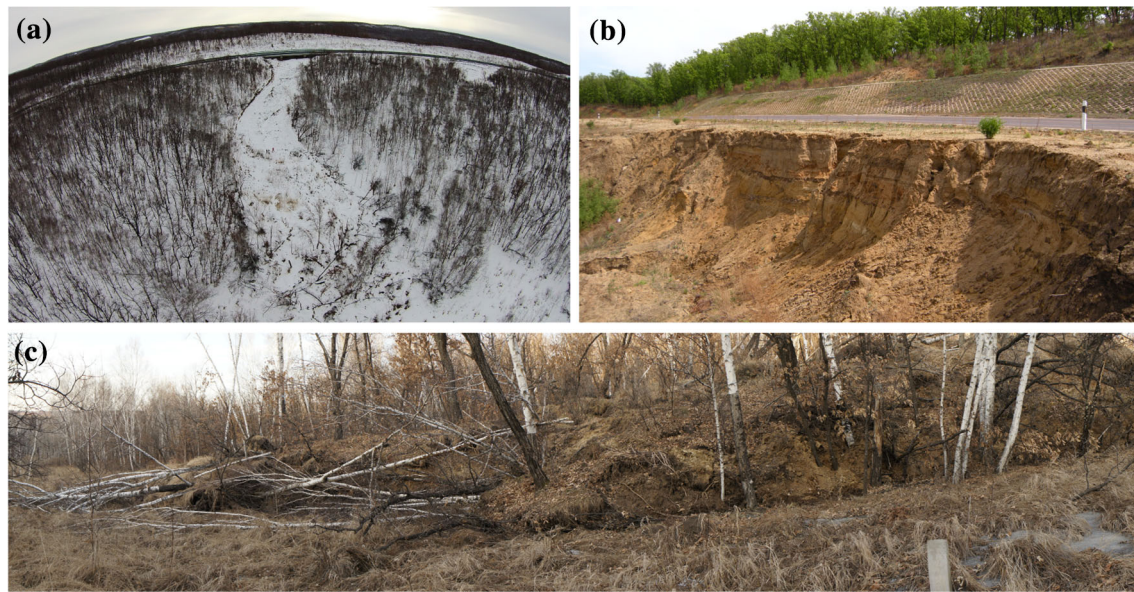


Fig. 2 Landslide scene photos. **a** Panoramic view of landslide (November 2014). **b** Trailing edge of landslide (June 2010). **c** Leading edge of landslide (October 2013)

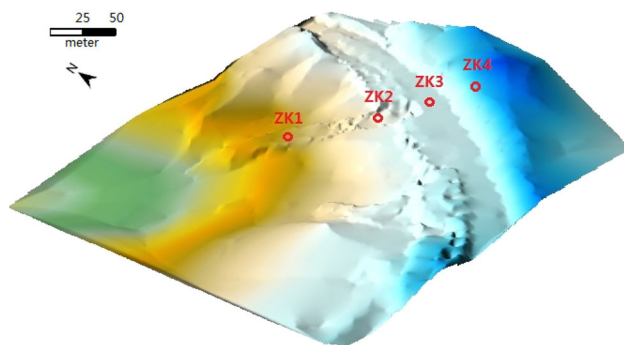


Fig. 3 Drilling borehole layout on landslide K178 + 530, and geomorphic map of the landslide area (drawn using SURFER software based on GPS terrain data in June 2010)

observed and calculated pseudo-sections using an iterative scheme. The smoothness constraint leads the algorithm to yield a solution with smooth resistivity changes. The pseudo-sections can be calculated by either finite-difference or finite-element methods (Coggon 1971; Dey and Morrison 1979). In this case, a finite-element scheme was employed due to the topographical changes in the field.

The smoothness-constrained least-squares method used in the inversion model is essentially a method in which the model resistivity is constantly adjusted through model correction in order to reduce the difference between the calculated apparent resistivity and the measured resistivity, and to describe the degree of fit between the two using the mean squared error. This method has been widely applied, and has a number of advantages, including adaptability to different types of data and models, a relatively small

influence of noise on the inversion data, high sensitivity to deep units, rapid inversion, and a small number of iterations. In tests using the HDR method, the spacing between unit electrodes was 3.0 m, and the maximum exploration depth of the survey lines was 30 m.

On the road section of landslide K178 + 530, a total of three HDR survey lines, I–I', II–II' and III–III', were established, as shown in Fig. 4. The measuring date was 3 September 2012.

GPR method

The GPR instrument used was the RIS-K2 FastWave Ground Penetrating Radar (IDS Ingegneria Dei Sistemi S.p.A., Pisa, Italy). The radar antenna was a low-frequency 40-MHz unshielded dual antenna. The detection time window was set to 600 ns, the sampling rate to 1024, and the data acquisition track pitch was 0.05 m. Two GPR survey lines were established, as shown in Fig. 4, with positions coinciding with those of the HDR survey lines, but with different start and end points. The two survey lines (I–I' and II–II') were 150 and 118 m in length, respectively. The date of measurement was 1 October 2013. GPR raw data were processed using REFLEXW scientific software (Sandmeier geophysical research, Karlsruhe, Germany). Coordinates for each trace were calculated at equal distances. The surface signal reflection was set to the zero-time position. Low frequencies and noise in the spectrum were filtered using a de-wow and bandpass filter. Next, temporally consistent signals were eliminated utilising background removal, and topographic correction was

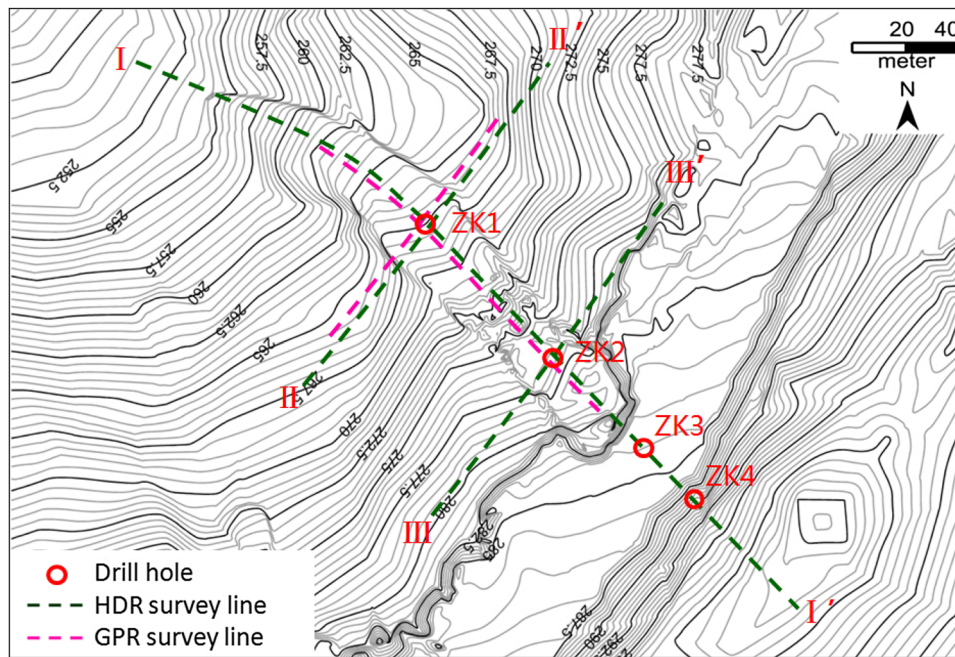


Fig. 4 Layout of the geophysical prospecting survey lines on landslide K178 + 530. (1) HDR survey lines: on the road section of landslide K178 + 530, a total of three HDR survey lines, I–I', II–II' and III–III', were established. Line I–I' ran along the slide direction of the landslide mass and passed through its center. The starting point of the survey line was located 40 m from the leading edge of the landslide mass, and the line sequentially passed through drilling boreholes ZK1, ZK2, ZK3 and ZK4. The total length of this survey line was 357 m (horizontal distance of 300 m). Line II–II' was perpendicular to the slide direction of the landslide mass, 110 m from the trailing edge, with point ZK1 serving as the midpoint, and electrodes

numbered 1–60 arranged in order from left to right. The total length of this survey line was 177 m. Line III–III' was perpendicular to the slide direction of the landslide mass, 50 m from the trailing edge, with point ZK2 serving as the midpoint, and electrodes numbered 1–60 arranged in order from left to right. The total length of this survey line was 177 m. The measuring date was 3 September 2012. (2) GPR survey lines: two survey lines were set up, with positions coinciding with those of the HDR survey lines, but with different start and end points. The GPR survey lines were shorter in length than the HDR survey lines. The two survey lines (I–I' and II–II') were 150 and 118 m long, respectively. The measuring date was 1 October 2013

applied. The picks were exported with the attribute of two-way travel time, and the velocity of propagation of the wave in this case appears to be about 0.10 m/ns.

Results, analysis and discussion

HDR

Survey line I–I'

The measured apparent electrical resistivity profile of line I–I' obtained on 3 September 2012 is shown in Fig. 5. The image shows that soil resistivity values of the landslide mass exhibited distinct layering. To better analyze how soil resistivity changes with depth, RES2DINV software can be used to extract the resistivity curve value of any point on the survey line. Figure 6 illustrates soil resistivity versus depth curves at boreholes ZK1 and ZK2. Taken together with the drilling result, changes in the characteristics of soil resistivity are analyzed as follows.

Borehole ZK1 is 115 m from the starting point of the HDR survey line. At a depth of 0–2.1 m, the soil is silty clay and rather loose, containing approximately 15 % grass roots and other organic matter. Resistivity values range from 25 to 45 Ohm m. At a depth of 2.1–6.7 m, the soil is silty clay, and there are local weathered sand layers. Resistivity values range from 45 to 65 Ohm m. At a depth of 6.7–8.0 m, the soil is yellow mudstone. The permeability coefficient is small, and it is difficult for the water to infiltrate downward, forming a watertight layer, and water easily gathers here. The resistivity value is relatively low, 20–30 Ohm m. At a depth of 8.0–26 m, the soil is gray mudstone, close to or below the water table. The resistivity value is relatively low, 10–25 Ohm m. As shown in the curve, silty clay contacts mudstone at a depth of 6.7 m, and resistivity exhibits apparent layering, with a sudden decrease in resistivity value.

The borehole ZK2 is 175 m from the starting point of the survey line. At a depth of 0–4.5 m, the soil is rather loose. Resistivity values range from 45 to 80 Ohm m. The resistivity of the surface embankment soil dominated by

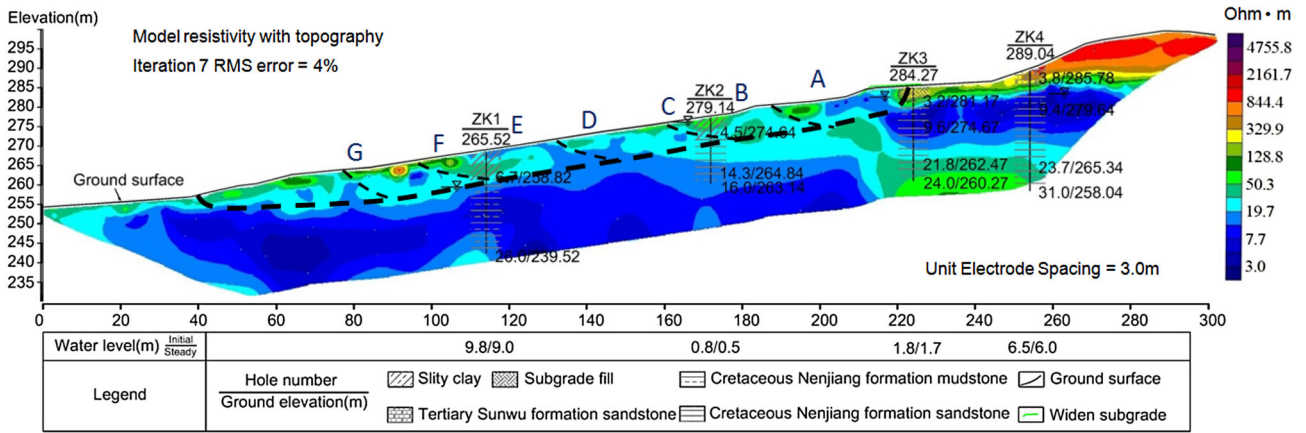


Fig. 5 Drilling results compared with electrical resistivity profile of survey line I-I'. Geological drilling date is June 2010; HDR detection date is 3 September 2012. The *thick black dashed line* show the

position of the major sliding surface, the thin *black dashed lines* show the secondary sliding surfaces. (see text for discussion)

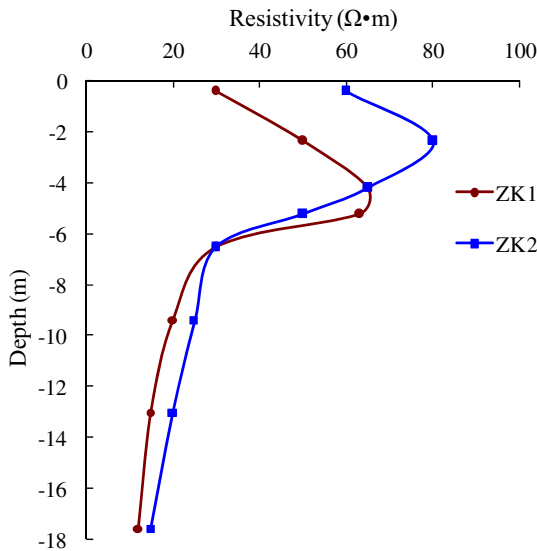


Fig. 6 Electrical resistivity curves at positions *ZK1* and *ZK2*

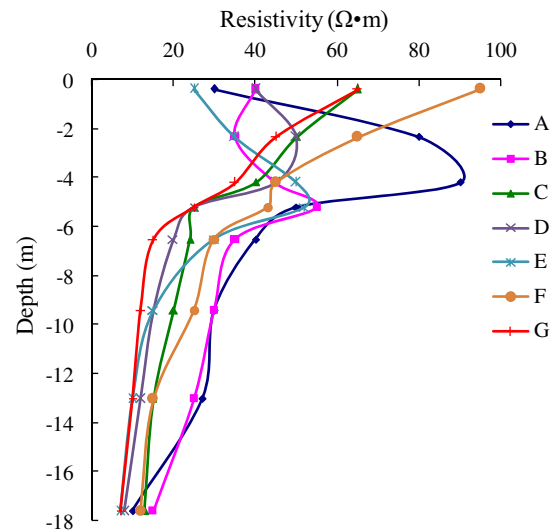


Fig. 7 Electrical resistivity curves at various points on survey line I-I'

silty clay (depth 0–3.8 m) ranges from 60 to 80 Ohm m, and that of gravelly sand (depth 3.8–4.5 m) ranges from 45 to 60 Ohm m. At a depth of 4.5–9.7 m, the soil is siltstone and composed of rather small particles. The permeability is poor, forming a watertight layer, with water easily gathering here. The resistivity value ranges from 25 to 35 Ohm m. At a depth of 9.7–14.6 m, the soil is sandstone, and resistivity values range from 15 to 25 Ohm m. As is evident in the curve, gravelly sand contacts siltstone at a depth of 4.5 m, and there is apparent resistivity layering, with a sudden decrease in resistivity value.

To better understand the changes in soil resistivity at different positions of line I-I', RES2DINV software was used to extract soil resistivity curves at points A, B, C, D, E, F and G on the survey line (Fig. 5). The horizontal

distances from A, B, C, D, E, F and G to the starting point of line I-I' are 80, 100, 120, 140, 160, 180 and 200 m, respectively. The soil resistivity curves obtained are shown in Fig. 7. At position A, the soil resistivity value decreases abruptly at a depth of 4.5 m. In other words, soil resistivity values at this depth exhibit abrupt stratification. We can thus determine that the sliding surface is located at a depth of 4.5 m. Similarly, the depths of the sliding surface at points B, C, D, E, F and G on line I-I' were determined to be 5, 4.7, 5.5, 6.5, 6, and 5.5 m, respectively.

The above-mentioned HDR profiles and resistivity curves show that soil resistivity values above and below the sliding surface of the landslide mass are clearly different and exhibit abrupt stratification. Based on this typical characteristic of the sliding surface, the positions of the

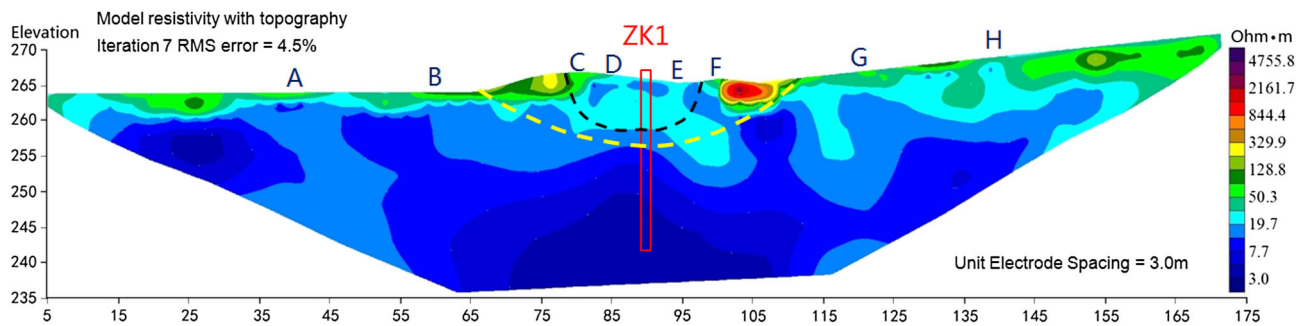


Fig. 8 Electrical resistivity profile of survey line II-II'. HDR detection date is 3 September 3 2012. The *black dashed line* shows the current sliding surface. The *yellow dashed line* shows the position of the sliding surface for the paleo-landslide

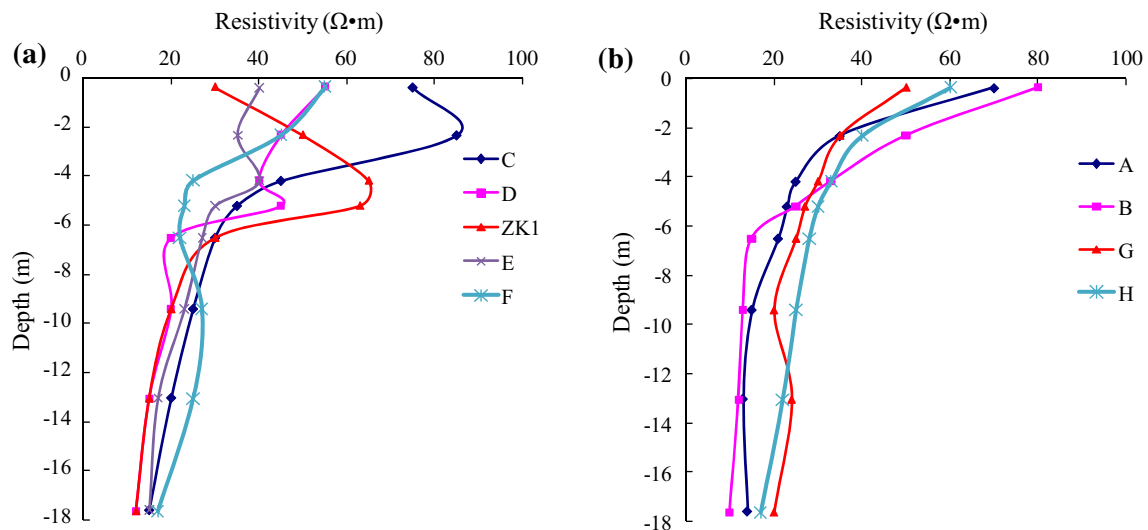


Fig. 9 Electrical resistivity curves at different points on survey line II-II' (points C, D, ZK1, E and F are all *on the landslide mass*; points A, B, G and H are all *outside the landslide mass*)

major sliding surfaces along line I-I' were deduced, as shown by the thick black dashed line in Fig. 5. The type of sliding for this landslide was characterized as propelled sliding, and the sliding power originated from the trailing edge of the landslide. The slip rate of the trailing edge was the greatest, followed by the middle part of the landslide; the minimum slip rate occurred at the leading edge (Shan et al. 2015). As a result, secondary sliding occurred in the landslide mass. By combining the changes in soil resistivity values for different positions in the landslide mass and drilling exploration, we obtained the secondary sliding surface, as shown by the thin black dashed line in Fig. 5.

Survey line II-II'

The measured apparent electrical resistivity profile of survey line II-II' is shown in Fig. 8, and the soil resistivity curves of points C, D, ZK1, E and F along line II-II' are

shown in Fig. 9a. The distances from C, D, ZK1, E and F to the starting point of the survey line are 80, 85, 90, 95 and 100 m, respectively. Based on Figs. 8 and 9a, we can determine the changes in soil resistivity value, which reveal apparent resistivity layering at the depths of the sliding surfaces, with a sudden decrease in resistivity value. Based on this characteristic of the sliding surface, the positions of the sliding surfaces along line II-II' were deduced, as shown by the black dotted line in Fig. 8. From the changes in soil resistivity values, we can infer that the depths of the sliding surfaces at positions C, D, ZK1, E and F on line II-II' are 4, 6, 6.5, 5.5 and 3.5 m, respectively. Figure 9b shows the soil resistivity curves of positions A, B, G and H (all outside the landslide mass) on survey line II-II'. The distances from A, B, G and H to the starting point of the survey line are 40, 60, 110 and 130 m, respectively. As can be seen in Fig. 9b, the soil resistivity values of the stable soil body outside the landslide showed

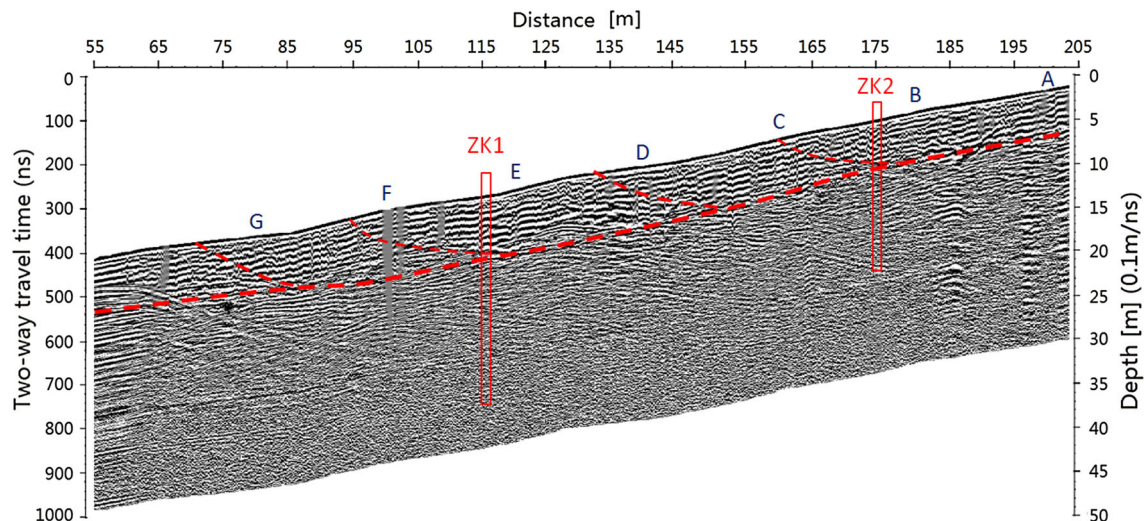


Fig. 10 GPR profile of survey line I–I'. The radar antenna is a low-frequency 40-MHz unshielded dual antenna; date of measurement is 1 October 1 2013. The *thick red dashed line* shows the position of the

stratification only in the loose surface layer. As depth increased, resistivity exhibited a largely monotonic decline, and there was no abrupt stratification.

This landslide belongs to a recurring old landslide that slipped again (Shan et al. 2015). The black dashed line in Fig. 8 shows the current sliding surface. Based on the site geological survey, combined with characteristics of resistivity changes, we can infer the position of the sliding surface for the paleo-landslide, as shown by the yellow dashed line in Fig. 8.

GPR

Survey line I–I'

The profile determined by the GPR survey line I–I' is illustrated in Fig. 10 (due to field constraints, this GPR survey line can only be used to measure this long section). The use of the layer picking option (phase follower) in the REFLEXW software can search continuous reflector, as shown in Fig. 10 (thick red dashed line). The intensity of the radar wave reflection differed significantly from that of the surrounding medium. The reflected wave signal is strong and shows distinctive horizon characteristics, presenting a low-frequency high-amplitude sync-phase axis, which can be inferred as the sliding surface. The continuity of the sliding surfaces is good, reflecting the depth range of the landslide mass development (Telford et al. 1990; Daniels 2004; Jol 2009).

With the use of REFLEXW radar data processing software, radar wave amplitude values can be extracted for all of the data acquisition track points in the profile at various depths. In order to better understand the changes in the

major sliding surface; the *thin red dashed lines* show the secondary sliding surfaces (see text for discussion)

intensity of the reflected radar waves, radar wave amplitude curves at positions A, B, ZK2, C, D, E, ZK1, F and G (as shown in Fig. 10) on survey line I–I' were plotted, as shown in Fig. 11. A higher radar wave amplitude indicates a greater intensity of the reflected radar wave (Telford et al. 1990; Benedetto et al. 2013). As can be seen in Fig. 11, because the surface soil body is rather loose in this area, most curves showed relatively large amplitudes in a depth range of 0–2.5 m. In position A, at a depth of 4.5 m, the radar wave amplitude increased substantially, exhibiting an abrupt change. Based on the characteristic differences in radar wave reflection among different types of soil bodies (Telford et al. 1990; Benedetto et al. 2013), we can infer that the soil moisture content in this position was relatively high, and thus the position of the sliding surface of the landslide mass can be deduced. Similarly, in positions B, ZK2, C, D, E, ZK1, F and G on line I–I', an abrupt increase in radar wave amplitudes occurred at depths of 4.7, 4.7, 5.5, 5.5, 6.7, 6.5, 5.6 and 5 m, respectively, and the position of the sliding surface can be inferred. This is very close to the position of the sliding surface as denoted by the thick red line in Fig. 10.

Survey line II–II'

The measured GPR profile of survey line II–II' is illustrated in Fig. 12. The red dotted line on the profile is the low-frequency high-amplitude sync-phase axis, and is determined to be the sliding surface of this profile, reflecting the depth range of the landslide mass development.

Using REFLEXW radar data processing software, we can obtain radar wave amplitude curves at positions A, B, C, D, ZK1, E, F, G and H (as shown in Fig. 12) on survey

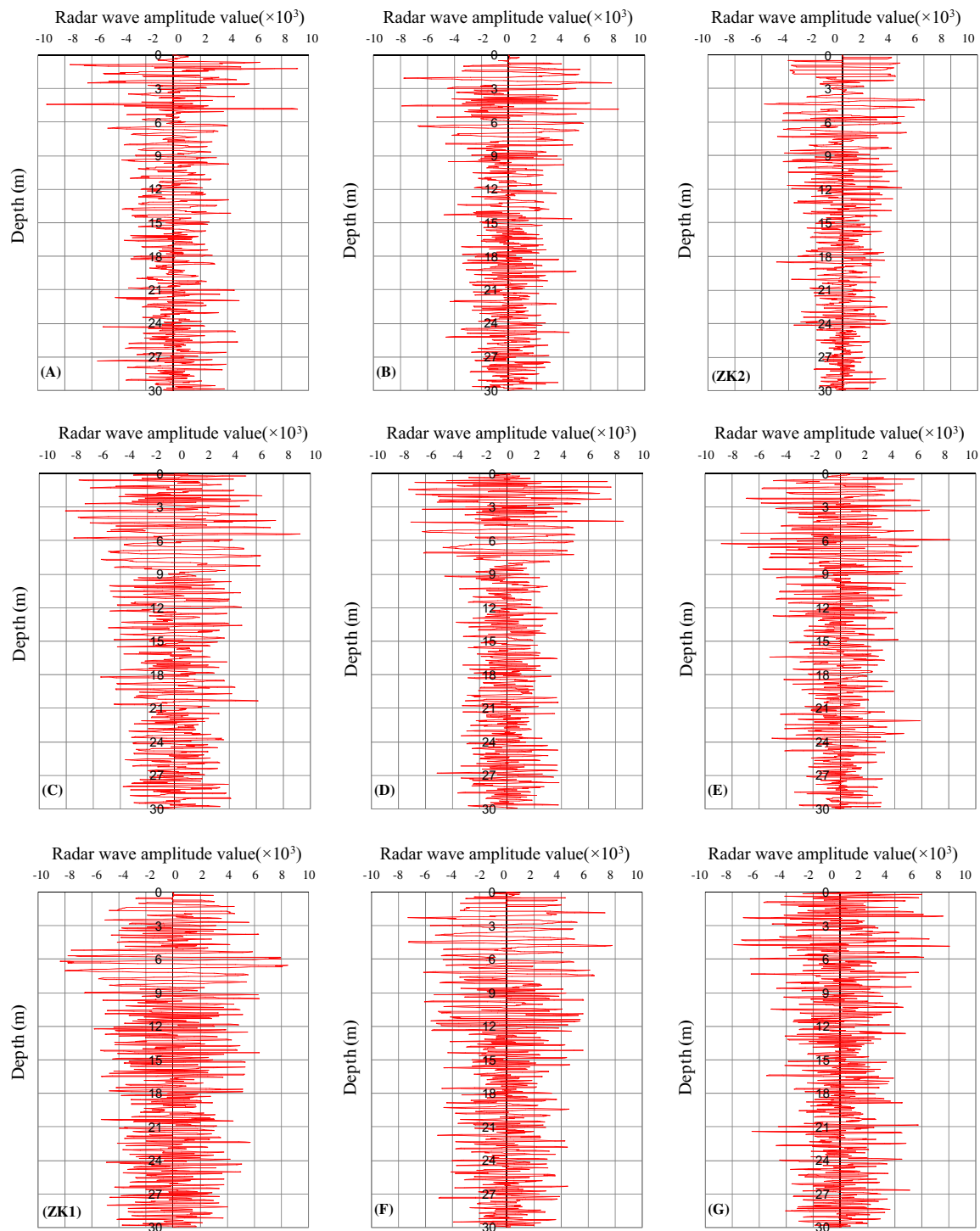


Fig. 11 Radar wave amplitude curves on survey line I-I'. Positions A, B, ZK2, C, D, E, ZK1, F and G are all on survey line I-I' (as shown in Fig. 10)

line II-II', as shown in Fig. 13. Here we can see that because the surface soil body is rather loose in this area, most curves show relatively large amplitudes in a depth range of 0–2.5 m. In positions D, ZK1 and E, which are all on the landslide mass, a sudden and substantial increase in

radar wave amplitude occurred at depths of 3.5, 6.5 and 3.2 m, respectively. Based on characteristic differences in radar wave reflection in different types of soil bodies (Telford et al. 1990; Benedetto et al. 2013), we can infer that the soil moisture content in this position is relatively

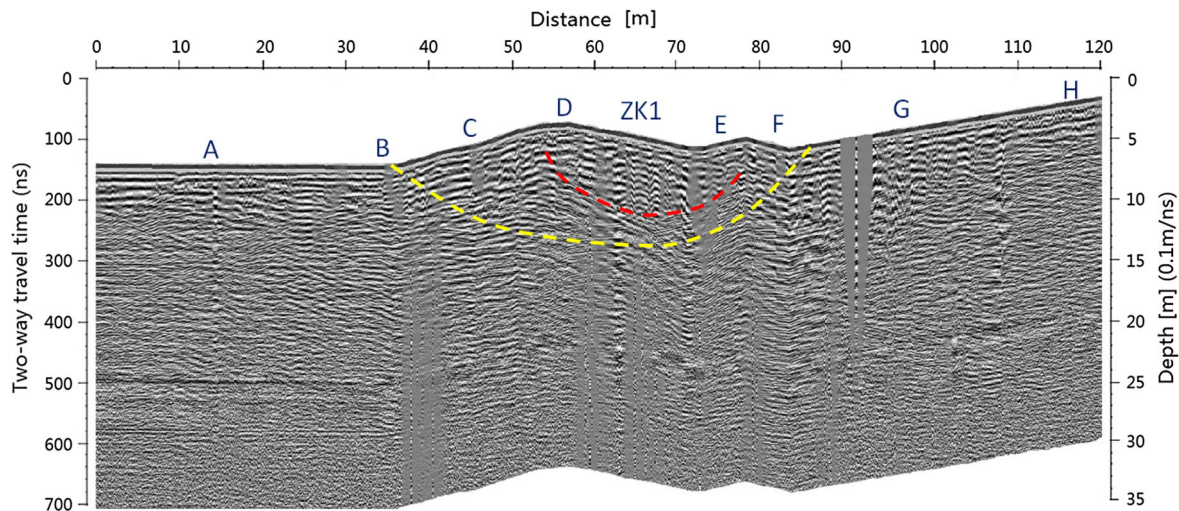


Fig. 12 GPR profile of survey line II–II'. GPR detection date is 1 October 1 2013. The *red dashed line* shows the current sliding surface. The *yellow dashed line* shows the position of the sliding surface for the paleo-landslide

high, and thus we can deduce the position of the sliding surface of the landslide mass. This position is about the same as that denoted by the red dashed line in Fig. 12. Positions A, B, G and H were all located outside the landslide mass. Abrupt changes in radar wave amplitude were exhibited only in the surface layer, i.e., at depths of 0–2.5 m; at greater depths, no abrupt changes were observed in radar wave amplitude curves.

As shown in Fig. 13, in positions C, D, ZK1, E and F, amplitude values were substantially increased, exhibiting abrupt change, at depths of 6, 9.5, 9, 7 and 3.5 m, respectively. These positions can be used to deduce the position of the sliding surface of the paleo-landslide, as denoted by the yellow dashed lines in Fig. 12. The magnitude of the abrupt change in radar wave amplitudes was smaller at the position of the sliding surface of the paleo-landslide than that of the current sliding surface.

The GPR results show that the moisture content of soils at the sliding surface of the landslide mass is relatively high. The drilling data also show very high moisture content of the sliding surface of the landslide mass in the study area, which is completely consistent with the results obtained from the GPR and HDR profiles.

Analysis of the mechanism underlying landslide development

In May 2010, a geological survey of the study area revealed permafrost in the shady slopes on the two sides of the landslides in this area (Shan et al. 2015). Permafrost was found by drilling on the profile of the survey line III–III', as shown in the permafrost soil sample photos in Fig. 14. In addition, the HDR method was used on 2 June

2010 for prospecting on the profile of survey line III–III'. Based on soil resistivity characteristics (Telford et al. 1990), we can infer the range of the permafrost layer on the profile of survey line III–III'. The measured apparent electrical resistivity profile of survey line III–III', obtained as of 2 June 2010, is shown in Fig. 15 (black dotted line).

As a result of permafrost melting and concentrated summer rainfall, soil slippage began at the end of July 2010, and the landslide was formed (Shan et al. 2015). Site surveys and borehole drilling data demonstrate that landslide K178 + 530 is a shallow creeping consequent landslide in the permafrost region. Water seepage generated by the melting of permafrost, together with water infiltration from concentrated summer precipitation, increases the local moisture content of the hillside soil. This is the main reason for landslide formation in the northwest region of the lesser Khingan range in China. Instability may easily occur in the rainy season and the spring melting season. The relatively large number of bulging cracks on the landslide mass allow water to easily accumulate and infiltrate downward. The highly permeable surface soil, gravel and sand layer, and silty clay containing a weathered sand interlayer provide a convenient channel for water infiltration. The mudstone and siltstone layers below have low permeability, forming watertight layers. Water generated from precipitation, melting snow and permafrost melting is blocked by the impermeable layer when it infiltrates downward, and the local moisture content increases sharply. Water thus infiltrates the interface between the permeable and impermeable layer, forming a slip zone. Using a combination of geophysical and drilling data, the position of the sliding surface can be determined, as shown by the red line in Fig. 16.

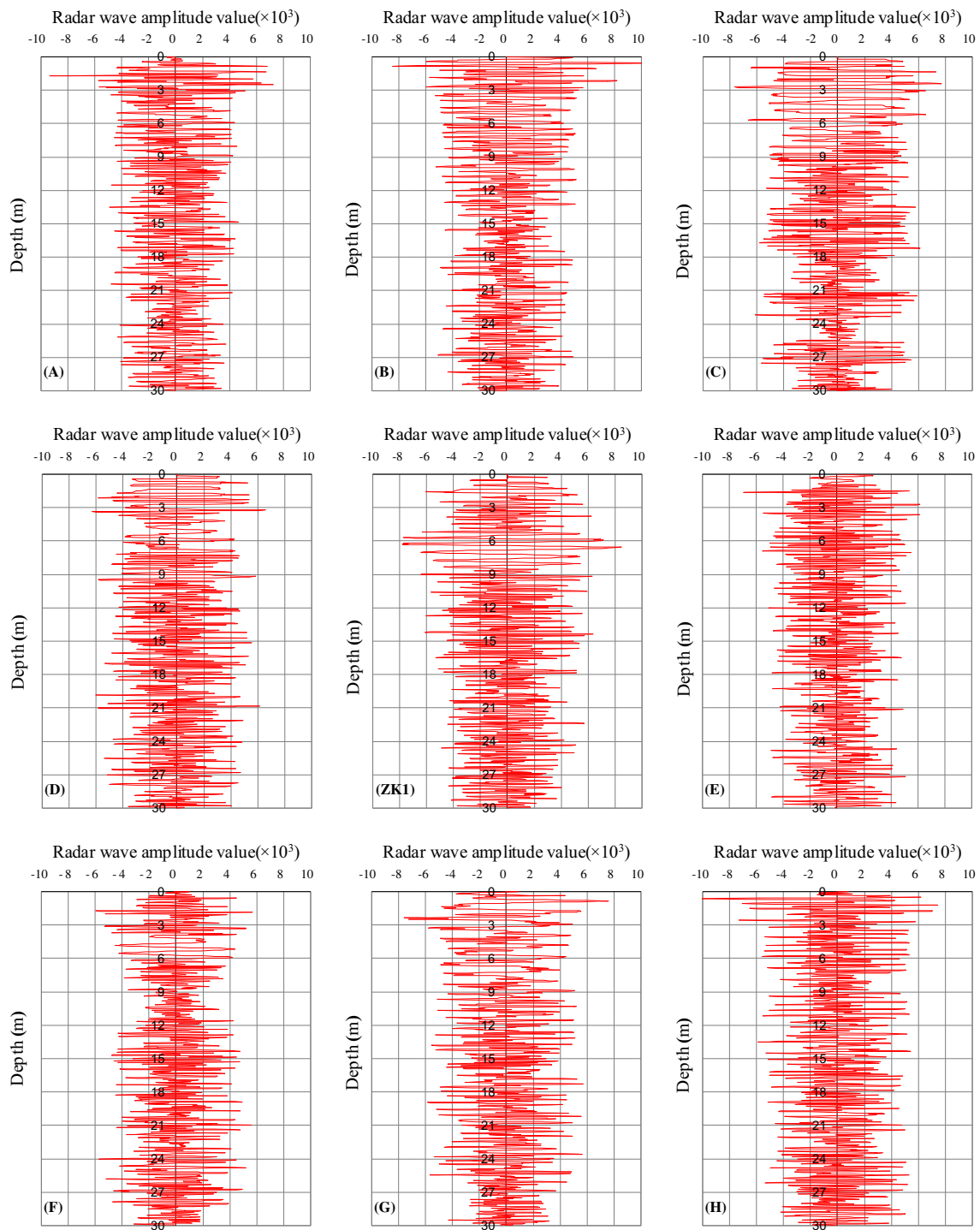


Fig. 13 Radar wave amplitude curves on survey line II–II'. Positions A, B, C, D, ZK1, E, F, G and H are all on survey line II–II' (as shown in Fig. 12)

Conclusions

Water seepage generated from the melting of permafrost, combined with the infiltration of concentrated summer precipitation, increases the local moisture content in the soil on hillsides, and is the main reason for landslide

formation in the northwest section of the lesser Khingan range in China. The landslide in the study area is a shallow creeping consequent landslide in the high-latitude permafrost region. The highly permeable surface soil, the sand and gravel layer, and the silty clay containing a weathered sand interlayer provide a convenient channel for water



Fig. 14 Photo of high-temperature permafrost. Sampling location is on survey line III–III', at the 40-m position on the *x*-axis. Drilling time is May 2010

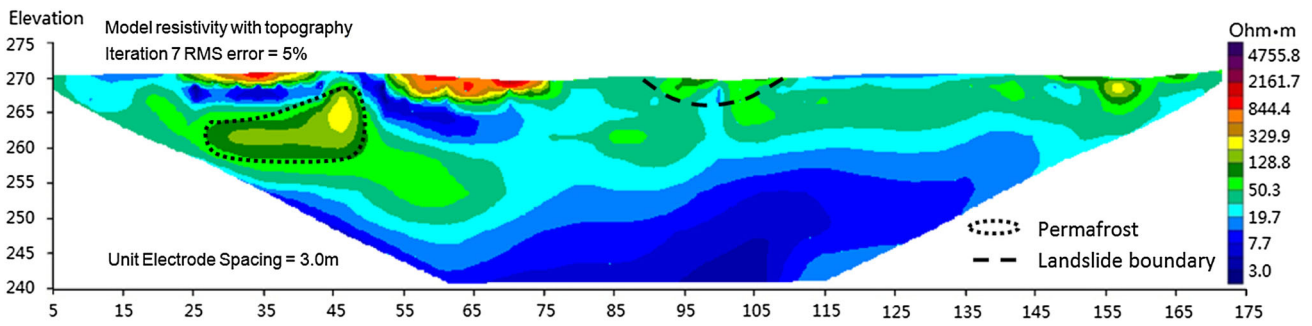


Fig. 15 Electrical resistivity profile of survey line III–III' (2 June 2010)

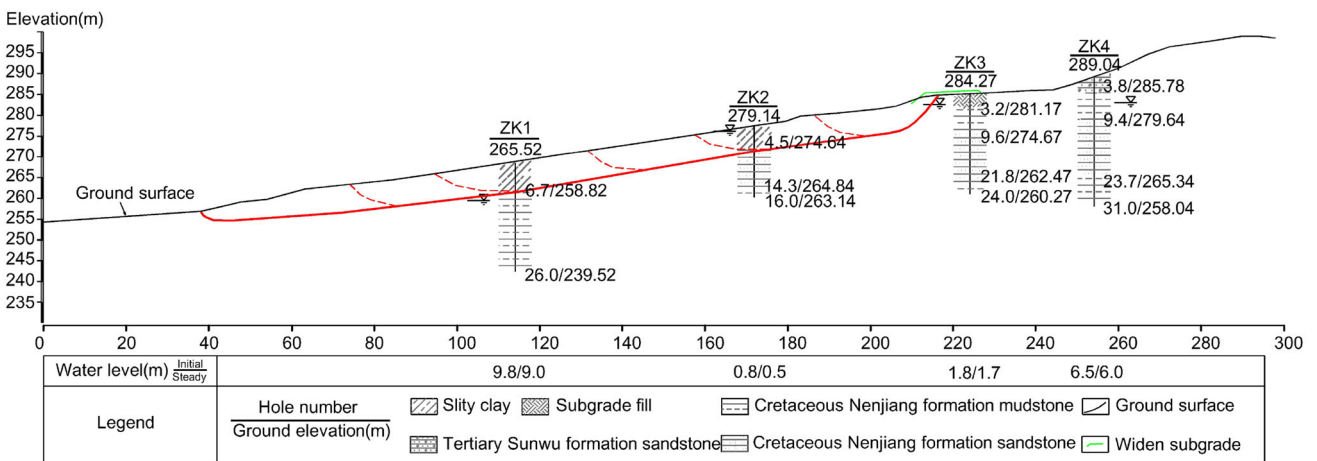


Fig. 16 Stratigraphic distribution of section K178 + 530 (*thick red dashed line* shows the position of the major sliding surface; *thin red dashed lines* show the secondary sliding surfaces)

infiltration, whereas the permeability of the mudstone and siltstone below is very low, forming a watertight layer. Water generated from permafrost melting, precipitation, melting snow and fractured springs rapidly increases the local water content as it infiltrates downward and along the

interface between the permeable and impermeable layers to form a slip zone.

Soil resistivity values above and below the sliding surface of the landslide mass are clearly different and exhibit an abrupt stratification. There is apparent resistivity

layering at the position of the sliding surface, with a sudden decrease in resistivity value. On the GPR profile, the sliding surface is manifested as a low-frequency, high-amplitude sync-phase axis, and there is a sudden increase in the amplitude of the radar wave. In practice, these abrupt, abnormal changes revealed in the HDR and GPR results can be used as characteristic markers for identifying the sliding surface position of shallow landslides in this region.

Prospecting of landslides in the study area using three methods, namely HDR, GPR and drilling, reveal basically the same sliding surface position, which suggests that HDR and GPR are fast, economical and reliable methods for site prospecting of landslides. They can be applied to shallow landslides in the high-latitude permafrost region for fast and accurate determination of the sliding surface position, providing a useful reference for engineering projects and for ensuring that appropriate measures are taken.

Acknowledgments This work was supported in part by the Science and Technology project of Chinese Ministry of Transport (No. 2011318223630) and the Fundamental Research Funds for the Central Universities (No. 2572014AB07).

Open Access This article is distributed under the terms of the Creative Commons Attribution 4.0 International License (<http://creativecommons.org/licenses/by/4.0/>), which permits unrestricted use, distribution, and reproduction in any medium, provided you give appropriate credit to the original author(s) and the source, provide a link to the Creative Commons license, and indicate if changes were made.

References

- Benedetto A, Benedetto F, Tosti F (2013) GPR applications for geotechnical stability of transportation infrastructures. *Nondestruct Test Eval* 27(3):253–262
- Bichler A, Bobrowsky P, Best M, Douma M, Hunter J, Calvert T, Burns R (2004) Three-dimensional mapping of a landslide using a multi-geophysical approach: the Quesnel Forks landslide. *Landslides* 1(1):29–40
- Cardarelli E, Marrone C, Orlando L (2003) Evaluation of tunnel stability using integrated geophysical methods. *J Appl Geophys* 52(2–3):93–102
- Carpentier S, Konz M, Fischer R, Anagnostopoulos G, Meusburger K, Schoeck K (2012) Geophysical imaging of shallow subsurface topography and its implication for shallow landslide susceptibility in the Urseren Valley, Switzerland. *J Appl Geophys* 83:46–56
- Coggon JH (1971) Electromagnetic and electrical modelling by the finite element method. *Geophysics* 36:132–155
- Daniels DJ (2004) Ground penetrating radar, 2nd edn. The Institution of Electrical Engineers, London
- Dey A, Morrison HF (1979) Resistivity modelling for arbitrarily shaped two-dimensional structures. *Geophys Prospect* 27:106–136
- Donohue S, Gavin K, Tolooiyan A (2011) Geophysical and geotechnical assessment of a railway embankment failure. *Near Surf Geophys* 9(1):33–44
- Drahor MG, Gokturkler G, Berge MA, Kurtulmus TO (2006) Application of electrical resistivity tomography technique for investigation of landslides: a case from Turkey. *Environ Geol* 50(2):147–155
- Hack R (2000) Geophysics for slope stability. *Surv Geophys* 21:423–448
- Havenith HB, Jongmans D, Abdrakhmatov K, Trefois P, Delvaux D, Torgoev A (2000) Geophysical investigations of seismically induced surface effects: case study of a landslide in the Suusamyr valley, Kyrgyzstan. *Surv Geophys* 21:349–369
- Jol HM (2009) Ground penetrating radar theory and applications. Elsevier, Amsterdam
- Loke MH, Barker RD (1996) Rapid least-squares inversion of apparent resistivity pseudosections using a quasi-Newton method. *Geophys Prospect* 44:131–152
- Malehmir A, Bastani M, Krawczyk CM, Gurk M, Ismail N, Polom U, Persson L (2013) Geophysical assessment and geotechnical investigation of quick-clay landslides—a Swedish case study. *Near Surf Geophys* 11(3):341–350
- McCann DM, Forster A (1990) Reconnaissance geophysical methods in landslide investigations. *Eng Geol* 29:59–78
- Perrone A, Lapenna V, Piscitelli S (2014) Electrical resistivity tomography technique for landslide investigation: a review. *Earth Sci Rev* 135:65–82
- Rhim CH (2011) Measurements of dielectric constants of soil to develop a landslide prediction system. *Smart Struct Syst* 7(4):319–328
- Sasaki Y (1992) Resolution of resistivity tomography inferred from numerical simulation. *Geophys Prospect* 40:453–463
- Sass O (2007) Bedrock detection and talus thickness assessment in the European Alps using geophysical methods. *J Appl Geophys* 62:254–269
- Sass O, Bell R, Glade T (2008) Comparison of GPR, 2D-resistivity and traditional techniques for the subsurface exploration of the Oschingen landslide, Swabian Alb (Germany). *Geomorphology* 93(1):89–103
- Sauvin G, Lecomte I, Bazin S, Hansen L, Vanneste M, LHeureux JS (2014) On the integrated use of geophysics for quick-clay mapping: the Hvittingfoss case study, Norway. *J Appl Geophys* 106:1–13
- Schrott L, Sass O (2008) Application of field geophysics in geomorphology: advances and limitations exemplified by case studies. *Geomorphology* 93:55–73
- Shan W, Hu Z, Guo Y, Zhang C, Wang C, Jiang H, Liu Y, Xiao J (2015) The impact of climate change on landslides in south-eastern of high-latitude permafrost regions of china. *Front Earth Sci* 3(7):1–11
- Telford WM, Geldart LP, Sheriff RE (1990) Applied geophysics, 2nd edn. Cambridge University Press, Cambridge
- Timothy S, Bilderback EL, Quigley MC, Nobes DC, Massey CI (2014) Coseismic landsliding during the M_w 7.1 Darfield (Canterbury) earthquake: implications for paleoseismic studies of landslides. *Geomorphology* 214:114–127
- Tripp AC, Hohmann GW Jr, Swift CM CM (1984) Two-dimensional resistivity inversion. *Geophysics* 49:1708–1717
- Yamakawa Y, Kosugi K, Masaoka N, Tada Y, Mizuyama T (2010) Use of a combined penetrometer-moisture probe together with geophysical methods to survey hydrological properties of a natural slope. *Vadose Zone J* 9(3):768–779
- Zajc M, Pogacnik Z, Gosar A (2014) Ground penetrating radar and structural geological mapping investigation of karst and tectonic features in flyschoid rocks as geological hazard for exploitation. *Int J Rock Mech Min Sci* 67:78–87